



## Axial-valley floor faults tell a different story than faults outside the axial valley: the role of dike-induced deformation

Jie Chen <sup>a,c,\*</sup>, Masako Tominaga <sup>b</sup>, Javier Escartín <sup>a</sup>

<sup>a</sup> Laboratoire de Géologie, Ecole Normale Supérieure/CNRS UMR 8538, PSL Research University, Paris 75005, France

<sup>b</sup> Department of Geology and Geophysics, Woods Hole Oceanographic Institution, Woods Hole, MA 02543, USA

<sup>c</sup> Now at School of Oceanography, Shanghai Jiao Tong University, Shanghai 200030, China

### ARTICLE INFO

Editor: Dr C Carolina Lithgow-Bertelloni

#### Keywords:

Slow-spreading ridges  
Autonomous underwater vehicle  
High-resolution bathymetry  
Dike-induced deformation  
Apparent tectonic strain  
ridge segmentation

### ABSTRACT

Slow-spreading ridges are highly segmented divergent plate boundaries with various modes of magma supply and faulting. Conventionally, magmatism and faulting that accommodate the plate divergence are thought to have an inverse relationship. However, our observations on fine-scale faulting, using high-resolution Autonomous Underwater Vehicle (AUV) bathymetry data along the axial-valley floor of the 14°N segment of the Mid-Atlantic Ridge, challenge this hypothesis. We show that axial faulting decreases from the segment center to the segment end as the rate of magma supply decreases and the lithosphere cools. This general pattern is also observed on several other slow-spreading ridge segments. We propose that this pattern relates to the link between fine-scale, newly-created axial faults and fissures and modes of magma supply. At segment centers, diking is frequent and centralized to the ridge axis, yielding strain localization and creating closely-spaced faults, whereas at segment ends, diking is less frequent and more widely distributed, yielding strain delocalization with faults distributed throughout the axial valley floor.

### Introduction

Seafloor spreading at mid-ocean ridges (MOR) is associated with magmatic and tectonic extension, creating oceanic lithosphere covering >2/3 of the Earth's surface. Faults accommodate tectonic plate divergence building prominent abyssal hills (Behn and Ito, 2008; Buck et al., 2005; Goff, 2020; Macdonald et al., 1996), associated with ubiquitous seismicity along the axis (Huang and Solomon, 1988; Olive and Escartín, 2016; Smith et al., 2003). Faults may also provide pathways for hydrothermal circulation that facilitate mass-energy exchanges between the hydrosphere and the lithosphere while sustaining ecosystems (Früh-Green et al., 2022). Understanding fault distribution and its origins at spreading axes is important to gain insights into how crustal accretion operates, and how crustal permeability structure can evolve and facilitate hydrothermal circulation during seafloor spreading (Behn et al., 2002; Chen et al., 2025, 2023; Cowie et al., 1993; Deschamps et al., 2007; Escartín et al., 2007, 1999).

To date, apparent tectonic strain (ATS) has been widely used as a proxy of the tectonic component of plate divergence ( $T$  value), with the magmatic component ( $M$  value) defined as  $M = 1 - T$  (Behn and Ito, 2008; Buck et al., 2005; Liu and Buck, 2020; Olive and Dublanchet, 2020; Shaw and Lin, 1996).

2020). ATS has typically been estimated by summing fault heaves along spreading flow lines, i.e., the horizontal offsets across faults, observed on the seafloor using ship-based bathymetry data with resolutions of 30–200 m/pixel (Carbotte and Macdonald, 1994; Escartín et al., 1999; Howell et al., 2016; Seale and Laughton, 1977). Analyses of off-axis abyssal-hill faults, over the timescales of a few millions of years, have shown that ATS generally increases with decreasing spreading rate or magma supply, and with axial lithosphere cooling and thickening (Carbotte and Macdonald, 1994; Escartín et al., 1999; Goff, 2020; Gracia, 1999; Howell et al., 2016). These observations are consistent with predictions from numerical models (Behn and Ito, 2008; Buck et al., 2005; Liu and Buck, 2020; Olive and Dublanchet, 2020; Shaw and Lin, 1996).

However, faulting operates over a wide range of spatiotemporal scales, and the possible links between faulting, tectonic strain, and magmatism over shorter timescales (e.g., 10s-100 s kyr) have rarely been investigated. A previous study reported that, at the young axial region, i.e. crust formed within the Brunhes normal period from the present to 780 kyr ago, ATS values estimated from high-resolution bathymetry data (1–2 m/pixel) at several MOR sites show no apparent correlation with spreading rate, melt supply, nor lithosphere structure

\* Corresponding author.

E-mail address: [chenjie.geo@sjtu.edu.cn](mailto:chenjie.geo@sjtu.edu.cn) (J. Chen).

(Chen et al., 2025). Faults formed near or at the ridge axis are thought to reflect dike-related deformation in the shallow lithosphere, in addition to tectonic extension (Carbotte et al., 2006; Marjanović et al., 2024), and may be buried by volcanic eruptions (Chen et al., 2021; Gini et al., 2021) and subsequently modified by mass wasting (Hughes et al., 2024). Upper-crustal volcanic processes render axial ATS time-dependent and spatially heterogeneous (e.g., affected by the extent of lava flows and zones of dike injection). Hence, ATS estimates may not accurately reflect the actual T value (Chen et al., 2025). In addition, at slow-spreading ridges, the spreading axis may migrate laterally within the axial valleys, resulting in asymmetries in faulting pattern (Chen et al., 2021; Escartín et al., 2014; Le Saout et al., 2023). To minimize observational bias and capture the ATS variability, fine-scale fault analyses using high-resolution bathymetry data should span the entire width of the axial valley, thereby enabling a comprehensive characterization of the axial faulting system.

In this paper, we systematically investigate the implications of axial faulting with respect to recent upper-crustal volcanic processes, along the axial-valley floor of the 14°N segment at the slow-spreading Mid-Atlantic Ridge (MAR). To achieve this, we use high-resolution bathymetry data (~1 m/pixel) collected by the Autonomous Underwater Vehicle (AUV) Sentry, operated by U.S National Deep Submergence Facility, during cruises AT33–03 in 2016 and AT40–02 in 2018 (Kurz et al., 2021). This segment is an ideal study area for two key reasons: (i) previous interpretation of along-axis melt distribution is that melt supply gradually decreases from the segment center to the ends (Smith et al., 2008), and (ii) axial fault systems of slow-spreading ridges may be better preserved than those at faster-spreading ridges, due to longer intervals between eruptions and the dominance of lower-effusion-rate hummocky lava flows rather than massive sheet flows covering existing fine-scale faults (Cann and Smith, 2005; Perfitt and Chadwick, 1998; Searle et al., 2010).

### Background: the MAR 14°N segment

The MAR 14°N segment is 70 km long, with a full spreading rate of ~27 km/Ma and bound by two non-transform discontinuities (NTD; Fig. 1) (Escartín and Cannat, 1999; Fujiwara et al., 2003; Smith et al.,

2008). This segment has low seismicity levels relative to adjacent ones based on the interpretations of teleseismic and hydroacoustic events (Fig. S1A) (Parnell-Turner et al., 2022; Smith et al., 2003). No hydrothermal venting has been detected to date along this segment, and the closest vent sites are located in the adjacent segments to the north and south, such as Logatchev, Semenov and Irinovskoe hydrothermal fields (Escartín et al., 2017; Gebruk et al., 2000). The axial valley is ~10 km wide along most of the central part of the segment (Fig. 1B). The crust inside the axial valley was formed during the Brunhes normal polarity period (i.e., 780 kyrs in Fig. 1) (Smith et al., 2008), with an estimated spreading age of ~400 kyrs. Rock samples dredged at the southern NTD include popping basalts that are geochemically enriched and contain CO<sub>2</sub>-filled bubbles (Bekaert et al., 2024; Jones et al., 2019; Péron et al., 2019).

Along the axial valley, the depth of the ridge axis at the segment center is ~880 shallower than that at the ends (Fig. 1A). The Mantle Bouguer gravity Anomaly (MBA) at the segment center is 28 mGal lower than at the ends (Fig. S1B), calculated using ship-based bathymetry (Fig. 1A) and the satellite-derived free-air gravity anomaly (Sandwell and Smith, 2009) (Fig. S1A; and see Methods in Supplementary). This along-axis variation corresponds to a gravity-derived estimate that indicates a relative crustal thickness of ~6.8 km at the segment center, which is ~1.4 km thicker than at the southern segment end, where the axis strikes at a ~45° from the spreading direction (Fig. 1C). Comparable variations in relative crustal thickness can also be observed along older isochrons off axis, e.g., along the 780 kyr isochron (Fig. 1C). These along-axis variations corresponds to the development of off-axis abyssal-hill faults that get increasingly prominent from the segment center to ends (Fig. 1B). In particular, an oceanic core complex (OCC) and its associated long-offset detachment fault have developed on the eastern flank of the southern end of the segment end at 13°50'N (Fig. 1B) (MacLeod et al., 2009; Parnell-Turner et al., 2018; Smith et al., 2008). Melt supply has thus been focused at the center of the MAR 14°N segment for a few million years, while segmentation was maintained. This along-axis variation in melt supply likely impacts the thermal state of the axial lithosphere, thickening from the segment center to the ends, a phenomenon commonly observed along slow-spreading ridge segments (Kuo and Forsyth, 1988; Lin et al., 1990).

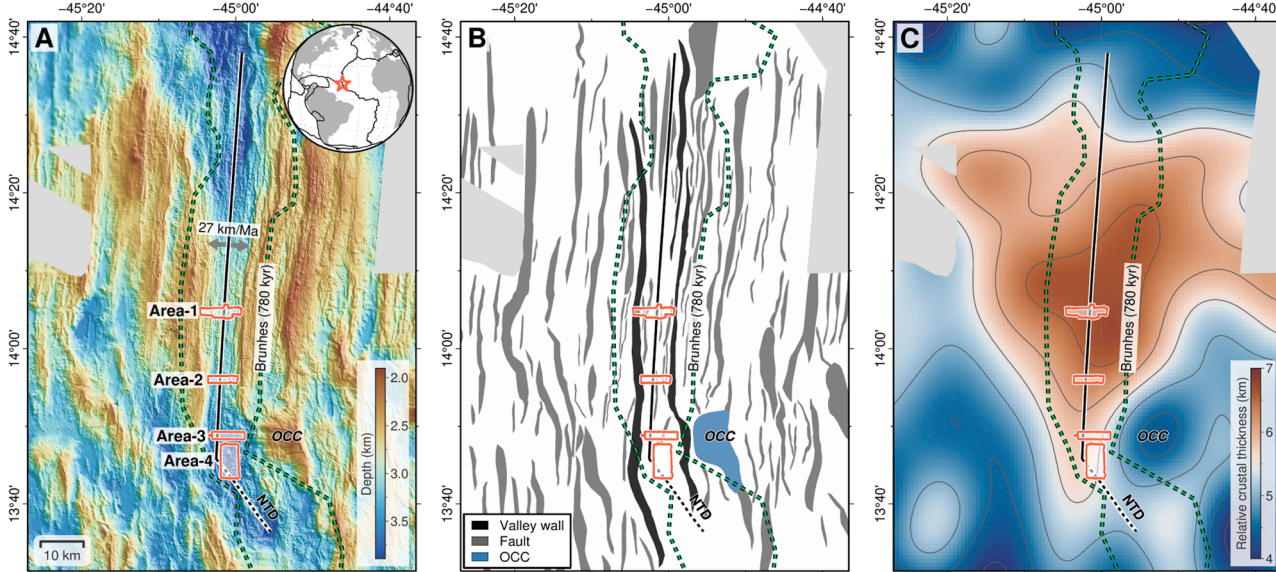


**Fig. 1.** The Mid-Atlantic Ridge (MAR) 14°N segment. (A) Ship-based bathymetry map. Areas mapped by Autonomous Underwater Vehicle (AUV) Sentry are outlined in black with a white transparency (1–4 from the segment center towards the southern end). Black solid and dashed lines mark the ridge axis and the non-transform discontinuity (NTD), respectively. Green dashed lines mark the magnetic picks of the Brunhes (i.e., the 780 kyr isochron) (Smith et al., 2008). (B) Geological interpretation of the valley wall, faults, and an oceanic core complex (OCC). (C) Map of gravity-derived relative crustal thickness calculated in this study (See Methods in Supplementary), that is consistent with prior estimates (Smith et al., 2008).

The plate divergence at the MAR 14°N segment is primarily accommodated by magmatic extension, with tectonic extension being more predominated at the segment ends. We refer to this type of segment as a magmatic segment, in contrast to detachment faulting-dominated segments at slow-spreading ridges. At the center of the MAR 14°N segment, the axial lithosphere structure may be similar to that of other magmatic slow-spreading segment centers (Fig. S2B-S2H), such as the MAR Lucky Strike segment (Fig. S2B). This segment likely hosts a hot crustal mush zone beneath a 3–4 km thick brittle lithosphere. (Bohidar et al., 2024; Crawford et al., 2013; Singh et al., 2006). In contrast, at the southern end of the segment, the lithosphere structure is probably analogous to the adjacent MAR 13°20'N OCC (Parnell-Turner et al., 2021, 2017) or the Mount Dent OCC at the Mid-Cayman Spreading Center (Grevemeyer et al., 2019) (Fig. S2I and S2J), where the brittle lithosphere is up to >10 km thick with the absence of a crustal mush zone.

#### Methods and results: faulting pattern and apparent tectonic strain

High-resolution bathymetry data acquired with the AUV Sentry mapped four areas along the MAR 14°N segment (dives 376–379, 487, and 489 in Area-1, dives 481, 482, and 486 in Area-2, dives 374, 476, 479, 483, 484, and 488 in Area-3, and dives 371–373, 375, 473–475, 477, 478, 480, and 488 in Area-4; Fig. 2 and 3). From north to south, they are located at the segment center (Area-1), the mid-way between the segment center and the end (Area-2), the southern end of the segment (Area-3), and within the oblique southern NTD (Area-4), which are located 0, 16, 29, and 40 km to the south of the segment center (Fig. 4). Areas 1–3 cover most of the rift valley floor, while Area-4 mainly covers the eastern flank of the rift valley floor.

The methods we used to identify and map faults and fissures are described in the Supplementary Materials (Chen et al., 2025). 2554 fault scarps and 1190 open fissures were manually digitized as closed polygons (Fig. 3 and Table S1), based on bathymetry (Fig. 2) and slope maps (Fig. S3). We also measured several geometric parameters, i.e., fault relief, length, dip, and spacing. Fault relief ranges from 2 to 330 m, and

fault length varies between 10 and 3300 m. The cumulative frequency of maximum fault relief and fault length at the 4 areas follow exponential scaling laws, and their normalized distributions are consistent at reliefs of <40 m and lengths of <200 m (log-linear plots in Fig. S5). The ratios of maximum fault relief to fault length (i.e., D/L ratio) across the 4 areas are comparable, averaging 0.12 (Fig. S6), which falls within the range of a global compilation (Lathrop et al., 2022) (Fig. S6). The average spacing of faults and fissures increases from 110 m in Area-1 at the segment center, to 158 m in Area-2, and 164 m in Area-3, decreasing to 146 m in Area-4 at the southern oblique NTD.

To illustrate the spatial variability of apparent tectonic strain (ATS; Fig. 3), we calculate ATS maps based on a cumulative fault heave (derived from the measurements of individual fault relief and assuming a uniform fault dip of 65°) and a cumulative fissure width over a moving window with a search radius of 200 m; ATS values represent the percentage of area within the moving window that is occupied by faults and fissures (see Methods in Supplementary) (Chen et al., 2025). For comparison, other ATS estimates from different combinations of search radii (100 and 400 m) and fault dip (75°) are shown in Fig. S7.

Area-1 (Figs. 2A and 3A) is located at the segment center, and includes the rift valley floor and the base of the valley walls. Two hummocky axial volcanic ridges (AVR; 45°01'W) mark the volcanic axis, located slightly east of the middle point of the rift valley floor. The ‘tectonic axis’, referring to the zone where inward-facing faults converge and mark the transition in fault facing, cannot be clearly defined at Area-1 because the AVR is mostly unfaulted. Off the volcanic axis (i.e., the AVR), faults are predominantly inward facing, with a roughly symmetric pattern. The ATS map displays a pattern of multiple linear, ridge-parallel bands (Fig. 3A); two ATS bands follow along the conjugate valley walls, in addition to a narrow band to the east of the AVR, and a wide band to the west of the AVR. The seafloor on both flanks between these bands shows near-zero ATS.

Area-2 (Figs. 2B and 3B), located 16 km south of the segment center, includes the rift valley floor and parts of valley walls. Faults are predominantly inward facing with a well-defined tectonic ridge axis, which is located slightly west of the middle point of the valley floor. The valley floor exhibits no AVR, and there are no other features that clearly

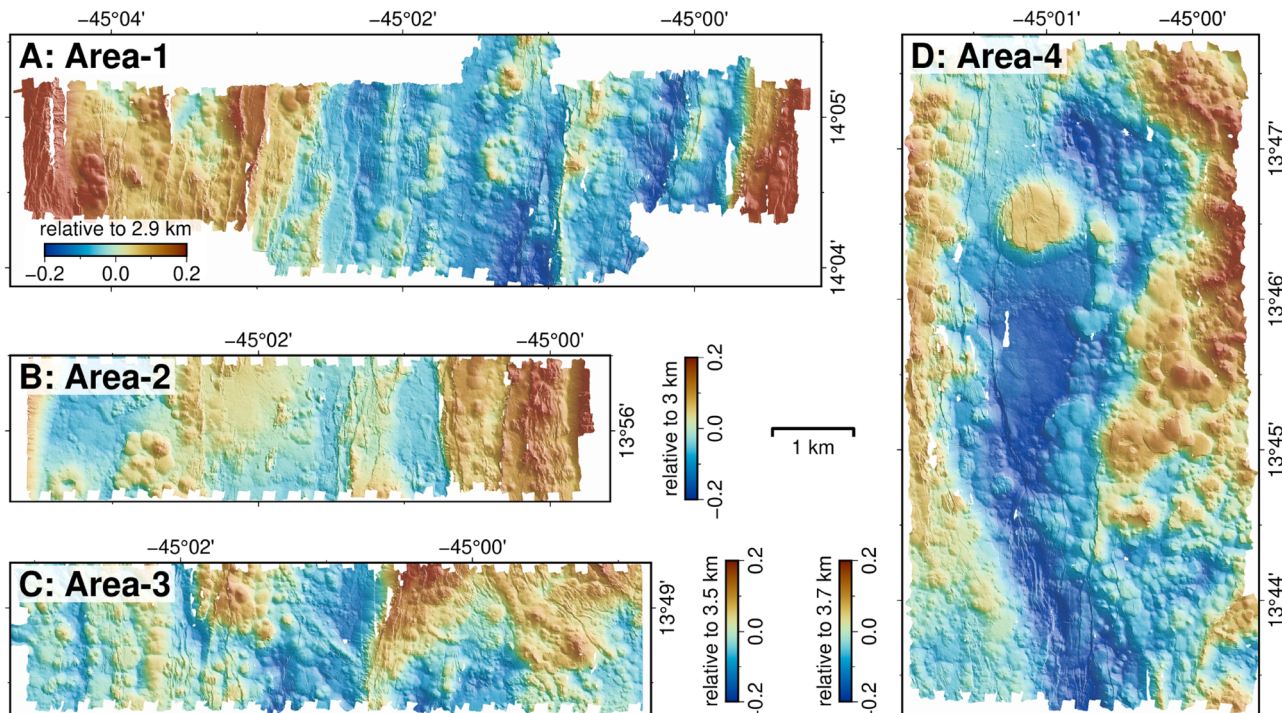


**Fig. 2.** AUV high-resolution bathymetry maps of the Areas 1–4. All maps are at the same scale and displayed with the same color bar for relative depths.

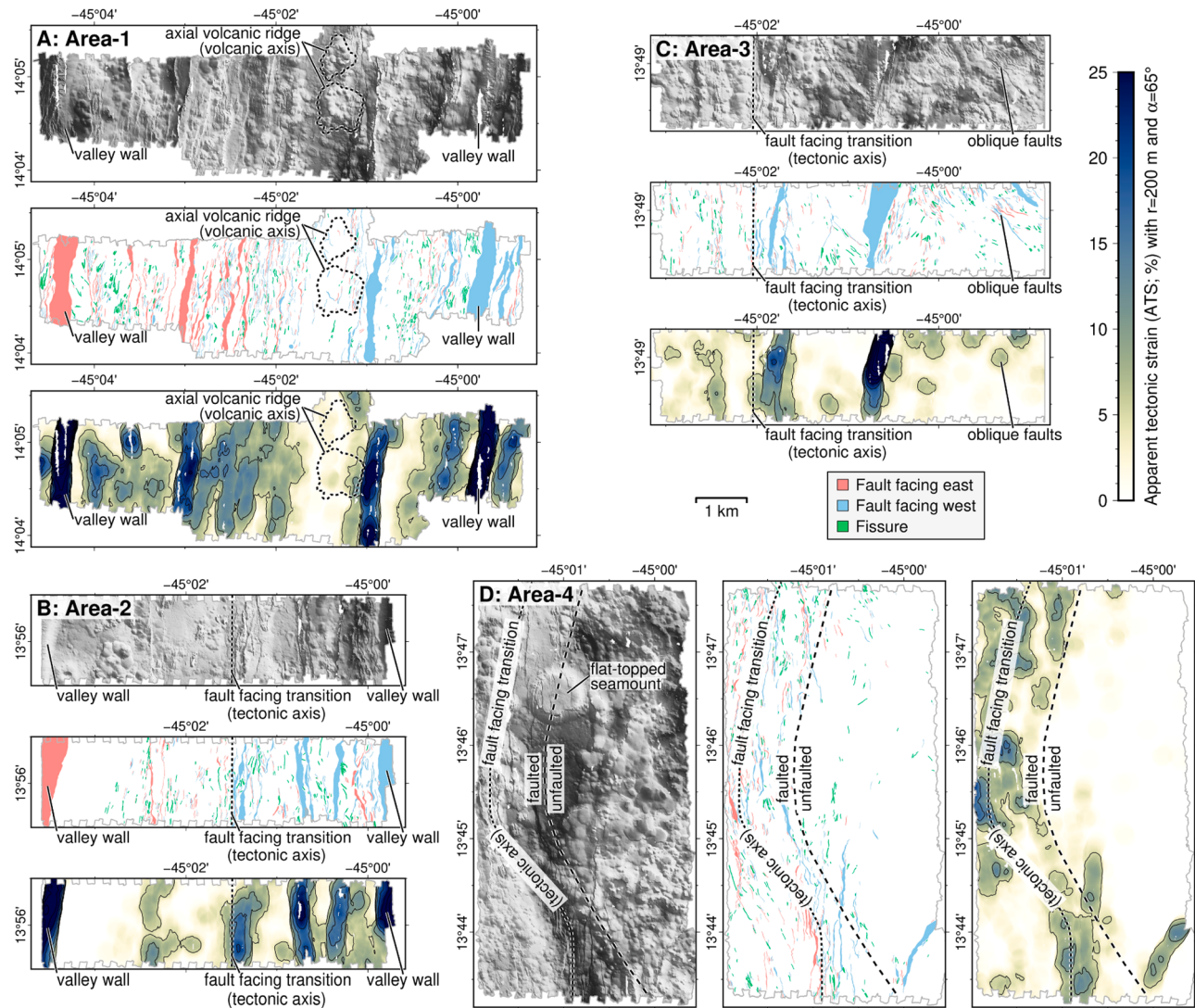


**Fig. 3.** Faulting pattern and apparent tectonic strain (ATS) in the valley floor the MAR 14°N segment, based on AUV high-resolution bathymetry data. (A) to (D) corresponds to Areas 1–4, respectively, each including a map of the bathymetry shown with shaded relief, interpretations of faults and fissures, and calculated ATS values. All maps are at the same scale. Axial volcanic ridge (interpreted as the volcanic axis), valley walls, and fault facing transition (interpreted as the tectonic axis) are indicated. East- and west-facing faults are indicated in red and blue, respectively, and fissures are shown in green. ATS is calculated using a fault dip and a search radius of  $\alpha = 65^\circ$  and  $r = 200$  m, respectively.

indicate the location of the volcanic axis. The faulting patterns are asymmetric, as the east flank displays both more faults and higher ATS values than west of the tectonic axis, where there is only one ATS band.

Area-3 (Figs. 2C and 3C) is located 29 km south of the segment center. The survey lies west of the 13°50'N OCC and excludes the valley walls. The fault-facing transition (tectonic axis) is located in the west of the mapped area. To the east of the fault-facing transition, the orientation of the faults and fissures rotates from NE20° (sub-perpendicular to the spreading direction) to NW50° (oblique), as it approaches the detachment fault on the flank. This rotation likely reflects the interaction between high-angle faults and detachment fault, with either stress rotation or a local shear of nearby lithosphere (Fig. 3C). The ATS map is characterized by three N-S bands and several scattered high value areas.

Area-4 (Figs. 2D and 3D) is located 40 km south of the segment center and mainly covers the eastern section of the valley floor within the oblique NTD. This features a striking area of unfaulted seafloor to the east, separated by a curved boundary from an adjacent area of faulted seafloor to the west. This boundary contains a curved transition that mimics the tectonic axis (with a divide between east- and west-facing faults, all inward-facing). The orientation of the faults and fissures is

nearly normal to the spreading direction, even though these faults have developed within the oblique-spreading NTD. The ATS map does not reveal ridge-parallel stripe patterns as in the prior study sites, but shows discontinuous, patchy areas with high ATS values (Fig. 3D). A rounded, flat-topped seamount with a diameter of 1.2 km is located on the fault/unfaulted boundary.

Our analysis also indicates that the ATS value, averaged within the rift valley for each area, gradually decreases from the segment center to the southern end, from 7.6 % in Area-1 to 5.1 % in Area-2, 4.3 % in Area-3, and 2.7 % in Area-4 (Fig. 4C). This along-axis trend aligns with the areal proportion of different ATS classes ( $>8$  %, 4–8 %, and  $<4$  %) in each site: the seafloor at the segment center (Area-1) is dominated by high ATS values ( $>8$  %), whereas low ATS values ( $<4$  %) become increasingly prevalent toward the segment end (Fig. S7A). We also calculate the fissure component of the average ATS inside the axial valley, which gradually decreases from 1.13 % in Area-1 to 1.02 % in Area-2, 0.82 % in Area-3, and 0.57 % in Area-4 (Fig. 4D).

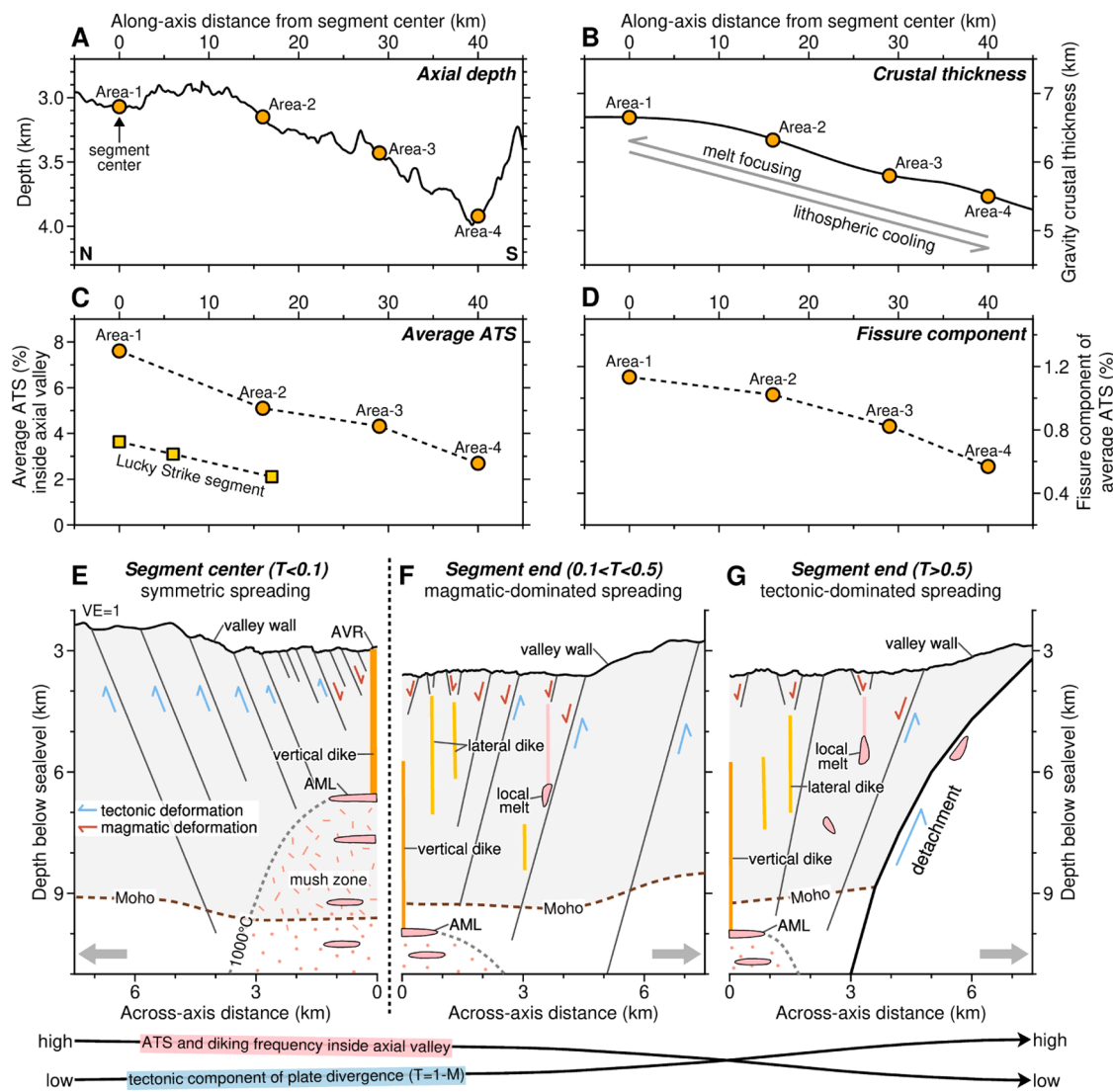


**Fig. 4.** Along-axis variations of diking-faulting systems at the MAR 14°N segment. (A) Along-axis depth profile with the locations of the study Areas 1–4. (B) Gravity-derived crustal thickness. (C) Average ATS, calculated using all faults and fissures inside the axial valley for the MAR 14°N segment. Yellow squares represent ATS measured along the Lucky Strike segment, using 2-m-resolution bathymetry with the same approach as in this study (Chen et al., 2025). (D) Fissure component of average ATS inside the axial valley along the MAR 14°N segment. (E)–(G) Schematic sketches (VE=1) of how diking-faulting systems are interpreted to vary from the segment center (Area-1) to the end (Area-3). The crust (gray), between the seafloor and Moho, is based on gravity-derived crustal thickness. Tectonic component of plate divergence ( $T = 1 - M$ ) increases from the segment center (E), magmatic-dominated segment end (F), to tectonic-dominated segment end with a detachment fault (G), while ATS and diking frequency inside axial valley decreases. Red and blue arrows represent faults related to magmatic and tectonic deformation, respectively. Dikes could originate from vertical propagation from AMLs (orange), lateral propagation (yellow), and local melt pockets (pink). Crystal mush zone is outlined by the 1000 °C isotherm (basaltic solidus), capped by axial melt lenses (AML).

## Discussion: axial ATS reflects dike-related deformation

Our fault analyses inside the rift valley along the magmatic MAR 14°N segment using AUV high-resolution bathymetry data indicate a gradual decrease in cumulative fault heave (i.e., the average ATS values) from the segment center to the southern end (Fig. 4C). This trend is consistent with that observed at other slow-spreading ridge sections surveyed with high-resolution bathymetry data, including the MAR Lucky Strike segment (Fig. 4C) (Chen et al., 2025), where, similarly, melt supply decreases and the lithosphere thickens from the segment center to the ends (Singh et al., 2006; Wang et al., 2025). As these data are acquired over the most recently accreted seafloor (within the rift valley), these correlations are thus representative of a short timescale, e.g., <1 Myrs, based on the width of the rift valley floor and the spreading rate.

In general, the ATS values are attributed to both the geometry and

distribution of the faults identifiable in a dataset, which in turn reflect its resolution and the scale of the geological processes it captures. One of the most prominent geological processes within the axial valley of a magmatic slow-spreading segment is axial rifting driven by dike events. Analogue (Corti et al., 2002) and numerical (Behn et al., 2006) models predict that the locus of magmatic accretion effectively controls surface deformation by localizing the strain in the overlying crust. As vertical blade-like dikes ascend close to the seafloor, they cause faulting near the dike tip, promoting strain localization and subsequent seafloor deformation and fault development (Chadwick and Embley, 1998; Head et al., 1996; Marjanović et al., 2024; Rubin, 1992). This process includes the formation of graben-like structures controlled by normal faults rooting at/near the dike tip (Rubin, 1992).

We propose that the axial ATS values are controlled by along-axis variations in diking frequency, which is ultimately and indirectly linked to melt supply. At the segment center, owing to a high melt supply

and enhanced volcanism, diking should decrease in frequency towards the segment ends, where melt supply is low relative to the segment center. In this scenario, faults and fissures in the rift valley floor may be primarily induced by diking, with volcanism unable to fully cover these structures. Notably, the fissure component of average ATS inside the axial valley along the MAR 14°N segment (Fig. 4D), which may directly reflect the diking process, as also observed in Iceland (Hjartardóttir et al., 2016; Rubin, 1992) and Mid-Ocean Ridges (Chadwick and Embrey, 1998; Wright et al., 2002), exhibits a decreasing pattern from the segment center to the end. These values may represent minimum estimates of dike-related strain along the ridge axis.

To further test our hypothesis, we revisited and made systematic evaluations of along-axis ATS variations around the centers of 8 magmatic slow-spreading segments (Fig. 5), using conventional ship-based bathymetry data with 50–150 m multi-resolution bathymetry grids (Ryan et al., 2009). We use the 14°N, Lucky Strike, Menez Gwen, 36°N, 35°N, 25°N segments of the MAR, the 23°S segment of the slow-spreading Central Indian Ridge (CIR), and the 50°E segment of ultraslow-spreading Southwest Indian Ridge (SWIR) (Fig. S2), the segment centers of which are influenced by enhanced magmatism. At each segment, five across-axis profiles were extracted at 5 km intervals along the ridge axis, with the central profile crossing the segment center and the others extending 10 km toward each segment end; each profile extends up to 20 km off axis on both flanks (Fig. S2 and S9). We calculated ATS values by: 1) summing fault reliefs along each across-axis profile (Fig. S10); 2) dividing by the profile length (40 km); 3) averaging the ATS values at the profiles with the same along-axis distance from the segment center on both sides of each segment (Fig. S11); and 4) normalizing with respect to the ATS at the segment center (equal to 1). The normalized ATS of 8 magmatic segments consistently peaks at the segment centers, with the most pronounced decreases occurring within 5 km away from segment centers along axis (Fig. 5). Notably, the maximum relief of bounding faults is also located at the segment centers, particularly in segments featuring rifted dome-shaped volcanoes, e.g., the

Menez Gwen, Lucky Strike, MAR 35°N, CIR 23°S, and SWIR 50°E segments (Fig. S2 and S9). A similar pattern of the ATS maxima at segment centers is also observed in subaerial volcanic spreading centers, such as the Dabbahu-Manda-Hararo segment of the East African Rift system (Dumont et al., 2019). We, therefore, propose that the axial ATS is not a proxy to evaluate the overall tectonic component of plate divergence (i.e., T value) over some spatiotemporal scales but rather reflects dike-induced faulting, and the pattern we observe in along-axis ATS variation inside the axial valley of the MAR 14°N segment is applicable to other magmatic segments.

We interpret that axial ATS values are indicative of the surface expression of dike-related deformation at very shallow crustal levels. At the segment centers with an overall T value typically  $< 0.1$  (Fig. 4E), dike injections, originating from a shallow mush zone capped by an axial melt lense (AML), are relatively frequent and localized within a narrow zone beneath the axial volcanic ridge. This leads to strain localization and the formation of symmetric, dike-induced faults that dissect central topographic highs. These dike-related faults are closely spaced (averaging to 110 m in Fig. 3A) and may extend to shallow crustal levels (Fig. 4E). Towards the segment ends, the frequency of dike injections decreases, due to reduced melt supply and the deepening of the AML (Fig. 4F and G). In addition, the rift valley widens, with dikes and associated AVRs becoming more diffuse, rather than concentrating in a narrow central zone (Chen et al., 2025; Escartín et al., 2014). It is unclear if these dikes originate from composite sources (Fig. 4F and G), which could propagate vertically from a deep AML and local melt pockets (Cannat, 1996); or, if they are emplaced by lateral propagation from the segment center (Grandin et al., 2012; Wang et al., 2025; Wright et al., 2006). The thick lithosphere at segment ends, together with a limited melt supply, can hinder dikes from reaching the seafloor to feed volcanic eruptions. Such a diffuse dike injection pattern can result in strain delocalization, potentially distributing dike-related faults throughout the entire axial valley floor (Fig. 4F and 4G). As a result, dike-induced faults at segment ends are fewer, asymmetric, and widely spaced (e.g., Fig. 3B and 3C), and they may root into deeper depths, as the lithosphere is colder and thicker.

The along-axis ATS variation observed within the axial valley does not conform to models that predict an increase of tectonic strain with distance along axis away from segment centers. In other words, the segment centers, where focused and/or enhanced magmatism occurs, are expected to have less tectonic extension of plate divergence than at the segment ends (Allerton et al., 1996; Escartín et al., 1999; Liu and Buck, 2020; Shaw and Lin, 1996). This expected pattern of tectonic strain is indeed observed when rift valley walls and off axis faults are considered (e.g., Fig. 1B), reflecting a longer-term tectonic accommodation of spreading, distinct from axial dike-related faults on shorter timescales.

Fig. 4E–G illustrate that there is a transition from axial faulting dominated by diking, to off-axis faulting with a balance between magmatic and tectonic deformation. As observed at the MAR 14°N segment (Fig. 1B), this off-axis tectonic deformation is likely to accommodate a greater portion of plate divergence (i.e., a higher T value) at the segment ends compared to the center, possibly resulting in more rapid off-axis fault growth at the segment ends, contributing to the formation of prominent off-axis abyssal hills or oceanic core complexes (Fig. 4F and G). A major conclusion of this study is that the causes and mechanisms of faulting within vs outside the axial valley at slow-spreading ridges are fundamentally different.

## Conclusions

High-resolution bathymetry data along the magmatic slow-spreading MAR 14°N segment show a decrease in the frequency of observable axial faulting from the segment center to the segment end. Although this trend is opposite to the conventionally understood inverse relationship between melt supply and tectonic strain, we demonstrate that this pattern

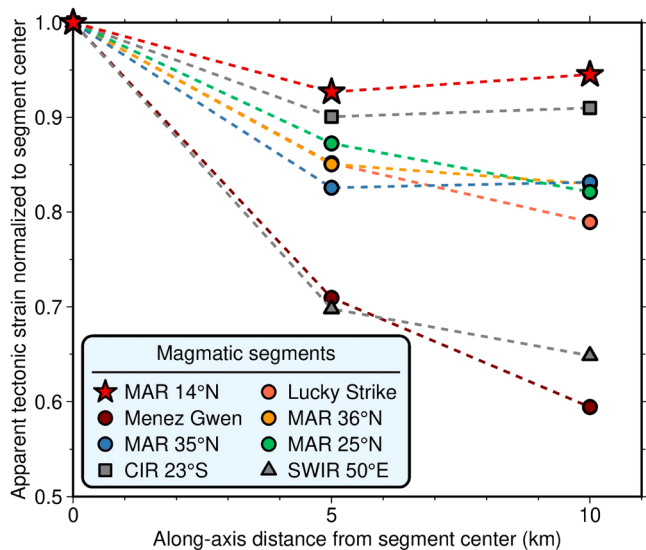


**Fig. 5.** Apparent tectonic strain (ATS) normalized to the centers of 8 magmatic slow-spreading ridge segments, based on ship-based bathymetry data. At each segment, five across-axis profiles were extracted at 5 km intervals along the ridge axis, with the central profile crossing the segment center and the others extending 10 km toward each segment end; each profile extends up to 20 km off axis on both flanks (Fig. S2 and S9). Each normalized ATS value is calculated by 1) summing fault reliefs along each across-axis profile (Fig. S10); 2) dividing by the profile length (40 km); 3) averaging the ATS values at the profiles with the same along-axis distance from the segment center on both sides of each segment (Fig. S11); and 4) normalizing with respect to the ATS at the segment center (equals to 1).

exists across several magmatic slow-spreading ridge segments. We interpret that the axial faults, observed in high-resolution bathymetry data reflect dike-related deformation in the shallow crust, rather than tectonic extension. This interpretation explains why the apparent tectonic strain (ATS) may not accurately estimate the tectonic component of plate divergence within the axial valley over short timescales. At the segment centers, ATS represents frequent and centralized dike injections that lead to strain localization at narrow grabens, whereas at the segment ends, ATS represents infrequent and distributed dike injections that lead to strain delocalization throughout the full width of the axial valley floor. This along-axis variations in diking-faulting at magmatic slow spreading ridges also creates high upper-crustal permeability at magma-enhanced segment centers, probably facilitating a focused upflow zone for hydrothermal fluids, e.g., the Lucky Strike hydrothermal vent (Barreyre et al., 2012).

#### Data availability

High-resolution bathymetry data at the MAR 14°N collected by the Sentry AUV are available at <https://doi.org/10.26022/IEDA/330198> (Kurz et al., 2021). Digital faults and fissures and calculated grid files of apparent tectonic strain are available at <https://doi.org/10.6084/m9.figshare.26510875>.

#### CRediT authorship contribution statement

**Jie Chen:** Writing – review & editing, Writing – original draft, Visualization, Validation, Software, Resources, Methodology, Investigation, Formal analysis, Conceptualization. **Masako Tominaga:** Writing – review & editing, Validation, Conceptualization. **Javier Escartín:** Writing – review & editing, Validation, Conceptualization.

#### Declaration of competing interest

The authors declare that they have no known competing financial interests or personal relationships that could have appeared to influence the work reported in this paper.

#### Acknowledgments

We gratefully acknowledge Mark Kurz, chief scientist of the AT33-03 and the AT40-02 cruises, the science party, the operation team of the Sentry AUV, and the crew of the R/V Atlantis for collecting the data used in this study. Jie Chen is funded by the ANR project "MUSH—OCEAN" (ANR-23-CE49-0013). Masako Tominaga is funded by WHOI IRD-28544. This paper also benefitted from constructive reviews by William Chadwick and an anonymous reviewer. Figures are generated using GMT-6 (Wessel et al., 2019).

#### Supplementary materials

Supplementary material associated with this article can be found, in the online version, at [doi:10.1016/j.epsl.2025.119796](https://doi.org/10.1016/j.epsl.2025.119796).

#### Data availability

I have shared the link to the data

#### References

- Allerton, S., Searle, R.C., Murton, B.J., 1996. Bathymetric segmentation and faulting on the Mid-Atlantic Ridge, 24°00'N to 24°40'N. *Geol. Soc. Spec. Publ.* 118, 49–60. <https://doi.org/10.1144/GSL.SP.1996.118.01.04>.
- Barreyre, T., Escartín, J., García, R., Cannat, M., Mittelstaedt, E., Prados, R., 2012. Structure, temporal evolution, and heat flux estimates from the Lucky Strike deep-sea hydrothermal field derived from seafloor image mosaics. *Geochem. Geophys. Geosystems* 13, Q04007. <https://doi.org/10.1029/2011GC003990>.
- Behn, M.D., Buck, W.R., Sacks, I.S., 2006. Topographic controls on dike injection in volcanic rift zones. *Earth Planet. Sci. Lett.* 246, 188–196. <https://doi.org/10.1016/j.epsl.2006.04.005>.
- Behn, M.D., Ito, G., 2008. Magmatic and tectonic extension at mid-ocean ridges: 1. Controls on fault characteristics. *Geochem. Geophys. Geosystems* 9, 8–10. <https://doi.org/10.1029/2008GC001965>.
- Behn, M.D., Lin, J., Zuber, M.T., 2002. Mechanisms of normal fault development at mid-ocean ridges. *J. Geophys. Res. Solid Earth* 107. <https://doi.org/10.1029/2001jb000503>.
- Bekaert, D.V., Barry, P.H., Curtice, J., Blusztajn, J., Hudak, M., Seltzer, A., Broadley, M. W., Krantz, J.A., Wanless, V.D., Soule, S.A., Mittelstaedt, E., Kurz, M.D., 2024. A carbon, nitrogen, and multi-isotope study of basalt glasses near 14°N on the Mid-Atlantic Ridge. Part B: mantle source heterogeneities. *Geochim. Cosmochim. Acta* 369, 179–195. <https://doi.org/10.1016/j.gca.2023.12.017>.
- Bohidar, S., Crawford, W.C., Cannat, M., 2024. Seismic constraints on hydrothermal circulation and magmatic-tectonic interactions beneath Lucky Strike Volcano, Mid-Atlantic Ridge. *Geochem. Geophys. Geosystems* 25, e2024GC011441. <https://doi.org/10.1029/2024GC011441>.
- Buck, W.R., Lavier, L.L., Poliakov, A.N.B., 2005. Modes of faulting at mid-ocean ridges. *Nature* 434, 719–723. <https://doi.org/10.1038/nature03358>.
- Cannat, J.R., Smith, D.K., 2005. Evolution of volcanism and faulting in a segment of the Mid-Atlantic Ridge at 25°N. *Geochem. Geophys. Geosystems* 6, Q09008. <https://doi.org/10.1029/2005GC000954>.
- Cannat, M., 1996. How thick is the magmatic crust at slow spreading oceanic ridges? *J. Geophys. Res. Solid Earth* 101, 2847–2857. <https://doi.org/10.1029/95jb03116>.
- Carbotte, S.M., Detrick, R.S., Harding, A., Canales, J.P., Babcock, J., Kent, G., Van Ark, E., Nedimovic, M., Diebold, J., 2006. Rift topography linked to magmatism at the intermediate spreading Juan de Fuca Ridge. *Geology* 34, 209–212. <https://doi.org/10.1130/G21969.1>.
- Carbotte, S.M., Macdonald, K.C., 1994. Comparison of seafloor tectonic fabric at intermediate, fast, and super fast spreading ridges: influence of spreading rate, plate motions, and ridge segmentation on fault patterns. *J. Geophys. Res. Solid Earth* 99, 13609–13631. <https://doi.org/10.1029/93jb02971>.
- Chadwick, W.W., Embley, R.W., 1998. Graben formation associated with recent dike intrusions and volcanic eruptions on the mid-ocean ridge. *J. Geophys. Res. Solid Earth* 103, 9807–9825. <https://doi.org/10.1029/97jb02485>.
- Chen, J., Cannat, M., Tao, C., Sauter, D., Munschy, M., 2021. 780 Thousand years of upper-crustal construction at a melt-rich segment of the ultraslow spreading Southwest Indian Ridge 50°28'E. *J. Geophys. Res. Solid Earth* 126, e2021JB022152. <https://doi.org/10.1029/2021JB022152>.
- Chen, J., Escartín, J., Cannat, M., 2025. Fault scarps and tectonic strain in young volcanic seafloor. *Earth Planet. Sci. Lett.* 651, 119174. <https://doi.org/10.1016/j.epsl.2024.119174>.
- Chen, J., Olive, J.A., Cannat, M., 2023. Beyond spreading rate: controls on the thermal regime of mid-ocean ridges. *Proc. Natl. Acad. Sci.* 120, e2306466120. <https://doi.org/10.1073/pnas.2306466120>.
- Corti, G., Bonini, M., Mazzarini, F., Boccaletti, M., Innocenti, F., Manetti, P., Mulugeta, G., Sokoutis, D., 2002. Magma-induced strain localization in centrifuge models of transfer zones. *Tectonophysics* 348, 205–218. [https://doi.org/10.1016/S0040-1951\(02\)00063-X](https://doi.org/10.1016/S0040-1951(02)00063-X).
- Cowie, P.A., Scholz, C.H., Edwards, M., Malinverno, A., 1993. Fault strain and seismic coupling on mid-ocean ridges. *J. Geophys. Res.* 98, 17911–17920. <https://doi.org/10.1029/93jb01567>.
- Crawford, W.C., Rai, A., Singh, S.C., Cannat, M., Escartín, J., Wang, H., Daniel, R., Combier, V., 2013. Hydrothermal seismicity beneath the summit of Lucky Strike volcano, Mid-Atlantic Ridge. *Earth Planet. Sci. Lett.* 373, 118–128. <https://doi.org/10.1016/j.epsl.2013.04.028>.
- Deschamps, J., Tivey, M., Embley, R.W., Chadwick, W.W., 2007. Quantitative study of the deformation at Southern Explorer Ridge using high-resolution bathymetric data. *Earth Planet. Sci. Lett.* 259, 1–17. <https://doi.org/10.1016/j.epsl.2007.04.007>.
- Dumont, S., Klinger, Y., Socquet, A., Escartín, J., Grandin, R., Jacques, E., Medynski, S., Doubre, C., 2019. Rifting processes at a continent-ocean transition rift revealed by fault analysis: example of Dabbahu-Manda-Hararo rift (Ethiopia). *Tectonics* 38, 190–214. <https://doi.org/10.1029/2018TC005141>.
- Escarthín, J., Cannat, M., 1999. Ultramafic exposures and the gravity signature of the lithosphere near the Fifteen-Twenty Fracture Zone (Mid-Atlantic Ridge, 14°–16.5°N). *Earth Planet. Sci. Lett.* 171, 411–424. [https://doi.org/10.1016/S0012-821X\(99\)00169-7](https://doi.org/10.1016/S0012-821X(99)00169-7).
- Escarthín, J., Cowie, P.A., Searle, R.C., Allerton, S., Mitchell, N.C., MacLeod, C.J., Slootweg, A.P., 1999. Quantifying tectonic strain and magmatic accretion at a slow spreading ridge segment, Mid-Atlantic Ridge, 29°N. *J. Geophys. Res. Solid Earth* 104, 10421–10437. <https://doi.org/10.1029/1998jb900097>.
- Escarthín, J., Mével, C., Petersen, S., Bonnemains, D., Cannat, M., Andreani, M., Augustin, N., Bezios, A., Chavagnac, V., Choi, Y., Godard, M., Haag, K., Hamelin, C., Ildefonse, B., Jamieson, J., John, B., Leleu, T., MacLeod, C.J., Massot-Campos, M., Nomikou, P., Olive, J.A., Paquet, M., Rommevaux, C., Rothenbeck, M., Steinbücher, A., Tominaga, M., Triebel, L., Campos, R., Gracias, N., García, R., 2017. Tectonic structure, evolution, and the nature of oceanic core complexes and their detachment fault zones (13°20'N and 13°30'N, Mid-Atlantic Ridge). *Geochem. Geophys. Geosystems* 18, 1451–1482. <https://doi.org/10.1002/2016GC006775>.
- Escarthín, J., Soule, S.A., Cannat, M., Fornari, D.J., Düsunür, D., García, R., 2014. Lucky Strike seamount: implications for the emplacement and rifting of segment-centered volcanoes at slow spreading mid-ocean ridges. *Geochem. Geophys. Geosystems* 15, 4157–4179. <https://doi.org/10.1002/2014GC005477>.
- Escarthín, J., Soule, S.A., Fornari, D.J., Tivey, M.A., Schouten, H., Perfit, M.R., 2007. Interplay between faults and lava flows in construction of the upper oceanic crust: the East Pacific Rise crest 9°25'–9°58'N. *Geochem. Geophys. Geosystems* 8, Q06005. <https://doi.org/10.1029/2006GC001399>.

- Früh-Green, G.L., Kelley, D.S., Lilley, M.D., Cannat, M., Chavagnac, V., Baross, J.A., 2022. Diversity of magmatism, hydrothermal processes and microbial interactions at mid-ocean ridges. *Nat. Rev. Earth Environ.* 3, 852–871. <https://doi.org/10.1038/s43017-022-00364-y>.
- Fujiwara, T., Lin, J., Matsumoto, T., Kelemen, P.B., Tucholke, B.E., Casey, J.F., 2003. Crustal evolution of the Mid-Atlantic Ridge near the Fifteen-Twenty Fracture Zone in the last 5 ma. *Geochem. Geophys. Geosystems* 4, 1024. <https://doi.org/10.1029/2002GC000364>.
- Gebruk, A.V., Chevaldonné, P., Shank, T., Lutz, R.A., Vrijenhoek, R.C., 2000. Deep-sea hydrothermal vent communities of the Logatchev area (14°45'N, Mid-Atlantic Ridge): diverse biotopes and high biomass. *J. Mar. Biol. Assoc. U. K.* 80, 383–393. <https://doi.org/10.1017/S0025315499002088>.
- Gini, C., Escartín, J., Cannat, M., Barreyre, T., 2021. Extrusive upper crust formation at slow-spreading ridges: fault steering of lava flows. *Earth Planet. Sci. Lett.* 576, 117202. <https://doi.org/10.1016/j.epsl.2021.117202>.
- Goff, J.A., 2020. Identifying characteristic and anomalous mantle from the complex relationship between abyssal hill roughness and spreading rates. *Geophys. Res. Lett.* 47, e2020GL088162. <https://doi.org/10.1029/2020GL088162>.
- Gracia, E., Bideau, D., Hekinian, R., Lagabrielle, Y., 1999. Detailed geological mapping of two contrasting second-order segments of the Mid-Atlantic Ridge between Oceanographer and Hayes fracture zones (33°30'N–35°N). *J. Geophys. Res. Solid Earth* 104, 22903–22921. <https://doi.org/10.1029/1999jb900161>.
- Grandin, R., Socquet, A., Doubre, C., Jacques, E., King, C.P., 2012. Elastic thickness control of lateral dyke intrusion at mid-ocean ridges. *Earth Planet. Sci. Lett.* 83–95. <https://doi.org/10.1016/j.epsl.2011.12.011>, 319–320.
- Grevemeyer, I., Hayman, N.W., Lange, D., Peirce, C., Papenberg, C., van Avendonk, H.J.A., Schmid, F., de la Peña, L.G., Dannowski, A., 2019. Constraining the maximum depth of brittle deformation at slow-and ultraslow-spreading ridges using microseismicity. *Geology* 47, 1069–1073. <https://doi.org/10.1130/G46577.1>.
- Head, J.W., Wilson, L., Smith, D.K., 1996. Mid-ocean ridge eruptive vent morphology and substructure: evidence for dike widths, eruption rates, and evolution of eruptions and axial volcanic ridges. *J. Geophys. Res. B Solid Earth* 101, 28265–28280. <https://doi.org/10.1029/96jb02275>.
- Hjartardóttir, Á.R., Einarsson, P., Gudmundsson, M.T., Högnadóttir, T., 2016. Fracture movements and graben subsidence during the 2014 Bárðarbunga dike intrusion in Iceland. *J. Volcanol. Geotherm. Res.* 310, 242–252. <https://doi.org/10.1016/j.jvolgeores.2015.12.002>.
- Howell, S.M., Ito, G., Behn, M.D., Martinez, F., Olive, J.-A., Escartín, J., 2016. Magmatic and tectonic extension at the Chile Ridge: evidence for mantle controls on ridge segmentation. *Geochem. Geophys. Geosystems* 17, 2354–2373. <https://doi.org/10.1002/2016GC006380>.
- Huang, P.Y., Solomon, S.C., 1988. Centroid depths of Mid-Ocean Ridge earthquakes: dependence on spreading rate. *J. Geophys. Res. Solid Earth* 93, 13445–13477. <https://doi.org/10.1029/JB093iB11p13445>.
- Hughes, A., Olive, J.-A., Malatesta, L.C., Escartín, J., 2024. Characterization of bedrock mass-wasting at fault-bound abyssal hills. *Earth Planet. Sci. Lett.* 648, 119073. <https://doi.org/10.1016/j.epsl.2024.119073>.
- Jones, M.P., Wanless, V.D., Soule, S.A., Kurz, M.D., Mittelstaedt, E., Fornari, D.J., Curtice, J., Klein, F., Le Roux, V., Brodsky, H., Péron, S., Schwartz, D.M., 2019. New constraints on mantle carbon from Mid-Atlantic Ridge popping rocks. *Earth Planet. Sci. Lett.* 511, 67–75. <https://doi.org/10.1016/j.epsl.2019.01.019>.
- Kuo, B.Y., Forsyth, D.W., 1988. Gravity anomalies of the ridge-transform system in the South Atlantic between 31 and 34.5°S: upwelling centers and variations in crustal thickness. *Mar. Geophys. Res.* 10, 205–232. <https://doi.org/10.1007/BF00310065>.
- Kurz, M., Mittelstaedt, E., Wanless, D., 2021. Processed near-bottom bathymetry grids (netCDF format) for survey sites 1 to 5 from Sentry AUV dives at the Mid-Atlantic Ridge (AT40-02, 2018). Interdiscip. Earth Data Alliance IEDA. <https://doi.org/10.26022/IEDA/330198>.
- Lathrop, B.A., Jackson, C.A.L., Bell, R., Rotevatn, A., 2022. Displacement/length scaling relationships for normal faults; a review, critique, and revised compilation. *Front. Earth Sci.* 10, 907543. <https://doi.org/10.3389/feart.2022.907543>.
- Le Saout, M., van der Zwan, F.M., Schiebeler, C.K., Augustin, N., 2023. Magmatism at an ultra-slow spreading rift: high-resolution geomorphological studies of a Red Sea Rift segment in Hadarba Deep. *Front. Mar. Sci.* 10. <https://doi.org/10.3389/fmars.2023.1273574>.
- Lin, J., Purdy, G.M., Schouten, H., Sempere, J.-C., Zervas, C., 1990. Evidence from gravity data for focused magmatic accretion along the Mid-Atlantic Ridge. *Nature* 344, 627–632. <https://doi.org/10.1038/344627a0>.
- Liu, Z., Buck, W.R., 2020. Global trends of axial relief and faulting at plate spreading centers imply discrete magmatic events. *J. Geophys. Res. Solid Earth* 125. <https://doi.org/10.1029/2020JB019465> e2020JB019465-e2020JB019465.
- Macdonald, K.C., Fox, P.J., Alexander, R.T., Pockalny, R., Gente, P., 1996. Volcanic growth faults and the origin of Pacific abyssal hills. *Nature* 380, 125–129. <https://doi.org/10.1038/380125a0>.
- MacLeod, C.J., Searle, R.C., Murton, B.J., Casey, J.F., Mallows, C., Unsworth, S.C., Achenbach, K.L., Harris, M., 2009. Life cycle of oceanic core complexes. *Earth Planet. Sci. Lett.* 287, 333–344. <https://doi.org/10.1016/j.epsl.2009.08.016>.
- Marjanović, M., Chen, J., Escartín, J., Parnell-Turner, R., Wu, J.-N., 2024. Magma-induced tectonics at the East Pacific Rise 9°50'N: evidence from high-resolution characterization of seafloor and subseafloor. *Proc. Natl. Acad. Sci.* 121. <https://doi.org/10.1073/pnas.2401440121> e2401440121–e2401440121.
- Olive, J.-A., Dublanchet, P., 2020. Controls on the magmatic fraction of extension at mid-ocean ridges. *Earth Planet. Sci. Lett.* 549, 116541. <https://doi.org/10.1016/j.epsl.2020.116541>.
- Olive, J.-A., Escartín, J., 2016. Dependence of seismic coupling on normal fault style along the Northern Mid-Atlantic Ridge. *Geochem. Geophys. Geosystems* 17, 4128–4152. <https://doi.org/10.1002/2016GC006460>.
- Parnell-Turner, R., Mittelstaedt, E., Kurz, M.D., Jones, M.P., Soule, S.A., Klein, F., Wanless, V.D., Fornari, D.J., 2018. The final stages of slip and volcanism on an oceanic detachment fault at 13°48'N, Mid-Atlantic Ridge. *Geochem. Geophys. Geosystems* 19, 3115–3127. <https://doi.org/10.1029/2018GC007536>.
- Parnell-Turner, R., Smith, D.K., Dziak, R.P., 2022. Hydroacoustic monitoring of seafloor spreading and transform faulting in the Equatorial Atlantic Ocean. *J. Geophys. Res. Solid Earth* 127, e2022JB024008. <https://doi.org/10.1029/2022JB024008>.
- Parnell-Turner, R., Sohn, R.A., Peirce, C., Reston, T.J., MacLeod, C.J., Searle, R.C., Simão, N.M., 2021. Seismicity trends and detachment fault structure at 13°N, Mid-Atlantic Ridge. *Geology* 49, 320–324. <https://doi.org/10.1130/G48420.1>.
- Parnell-Turner, R., Sohn, R.A., Peirce, C., Reston, T.J., MacLeod, C.J., Searle, R.C., Simão, N.M., 2017. Oceanic detachment faults generate compression in extension. *Geology* 45, 923–926. <https://doi.org/10.1130/G39232.1>.
- Perfit, M.R., Chadwick, W.W., 1998. Magmatism at mid-ocean ridges: constraints from volcanological and geochemical investigations. *Geophys. Monogr. Ser.* 106, 59–115. <https://doi.org/10.1029/GM106p0059>.
- Péron, S., Moreira, M.A., Kurz, M.D., Curtice, J., Blusztajn, J.S., Putlitz, B., Wanless, V.D., Jones, M.P., Soule, S.A., Mittelstaedt, E., 2019. Noble gas systematics in new popping rocks from the Mid-Atlantic Ridge (14°N): evidence for small-scale upper mantle heterogeneities. *Earth Planet. Sci. Lett.* 519, 70–82. <https://doi.org/10.1016/j.epsl.2019.04.037>.
- Rubin, A.M., 1992. Dike-induced faulting and graben subsidence in volcanic rift zones. *J. Geophys. Res.* 97, 1839–1858. <https://doi.org/10.1029/91JB02170>.
- Ryan, W.B.F., Carbotte, S.M., Coplan, J.O., O'Hara, S., Melkonian, A., Arko, R., Weissel, R.A., Ferrini, V., Goodwillie, A., Nitsche, F., Bonczkowski, J., Zemsky, R., 2009. Global Multi-Resolution topography synthesis. *Geochem. Geophys. Geosystems* 10. <https://doi.org/10.1029/2008GC002332>. Q03014.
- Sandwell, D.T., Smith, W.H.F., 2009. Global marine gravity from retracked Geosat and ERS-1 altimetry: ridge segmentation versus spreading rate. *J. Geophys. Res. Solid Earth* 114. <https://doi.org/10.1029/2008JB006008>. B01411.
- Searle, R.C., Laughton, A.S., 1977. Sonar studies of the Mid-Atlantic Ridge and Kurchatov Fracture Zone. *J. Geophys. Res.* 82, 5313–5328. <https://doi.org/10.1029/JB082i033p05313>.
- Searle, R.C., Murton, B.J., Achenbach, K., LeBas, T., Tivey, M., Yeo, I., Cormier, M.H., Carlu, J., Ferreira, P., Mallows, C., Morris, K., Schroth, N., van Calsteren, P., Waters, C., 2010. Structure and development of an axial volcanic ridge: mid-Atlantic Ridge, 45°N. *Earth Planet. Sci. Lett.* 299, 228–241. <https://doi.org/10.1016/j.epsl.2010.09.003>.
- Shaw, W.J., Lin, J., 1996. Models of ocean ridge lithospheric deformation: dependence on crustal thickness, spreading rate, and segmentation. *J. Geophys. Res. Solid Earth* 101, 17977–17993. <https://doi.org/10.1029/96jb00949>.
- Singh, S.C., Crawford, W.C., Carton, H., Seher, T., Combier, V., Cannat, M., Canales, J.P., Düsüür, D., Escartín, J., Miranda, J.M., 2006. Discovery of a magma chamber and faults beneath a Mid-Atlantic Ridge hydrothermal field. *Nature* 442, 1029–1032. <https://doi.org/10.1038/nature05105>.
- Smith, D.K., Escartín, J., Cannat, M., Tolstoy, M., Fox, C.G., Bohnenstiel, D.R., Bazin, S., 2003. Spatial and temporal distribution of seismicity along the northern Mid-Atlantic Ridge (15°–35°N). *J. Geophys. Res. Solid Earth* 108. <https://doi.org/10.1029/2002JB001964>, 2002JB001964.
- Smith, D.K., Escartín, J., Schouten, H., Cann, J.R., 2008. Fault rotation and core complex formation: significant processes in seafloor formation at slow-spreading mid-ocean ridges (Mid-Atlantic Ridge, 13°–15°N). *Geochem. Geophys. Geosystems* 9. <https://doi.org/10.1029/2007GC001699>. Q03003.
- Wang, Z., Singh, S.C., Minshull, T.A., Crawford, W.C., 2025. Fine-scale crustal velocity structure at the Lucky Strike segment of Mid-Atlantic ridge from full waveform inversion of wide-angle seismic data. *J. Geophys. Res. Solid Earth* 130. <https://doi.org/10.1029/2024JB029982> e2024JB029982.
- Wessel, P., Luis, J.F., Uieda, L., Scharroo, R., Bobbe, F., Smith, W.H.F., Tian, D., 2019. The generic mapping tools version 6. *Geochem. Geophys. Geosystems* 20, 5556–5564. <https://doi.org/10.1029/2019GC008515>.
- Wright, D.J., Haymon, R.M., White, S.M., Macdonald, K.C., 2002. Crustal fissuring on the crest of the southern East Pacific Rise at 17°15'–40'S. *J. Geophys. Res. Solid Earth* 107. <https://doi.org/10.1029/2001JB000544>.
- Wright, T.J., Ebinger, C., Biggs, J., Ayale, A., Yirgu, G., Keir, D., Stork, A., 2006. Magma-maintained rift segmentation at continental rupture in the 2005 Afar dyking episode. *Nature* 442, 291–294. <https://doi.org/10.1038/nature04978>.

## **Supplementary for**

### **Axial-valley floor faults tell a different story than faults outside the axial valley: the role of dike-induced deformation**

Jie Chen<sup>1,3</sup>, Masako Tominaga<sup>2</sup>, Javier Escartín<sup>1</sup>

<sup>1</sup> Laboratoire de Géologie, Ecole Normale Supérieure/CNRS UMR 8538, PSL Research University, Paris 75005, France

<sup>2</sup> Department of Geology and Geophysics, Woods Hole Oceanographic Institution, Woods Hole, MA 02543, USA

<sup>3</sup> Now at School of Oceanography, Shanghai Jiao Tong University, Shanghai 200030, China

Corresponding author: Jie Chen (chenjie.geo@outlook.com)

#### **This file includes:**

- Methods
- Table S1
- Fig. S1-S11

## Methods

### Gravity inversion at the MAR 14°N segment

Following the gravity inversion approach (Kuo and Forsyth, 1988; Lin et al., 1990), we first calculate the map of Mantle Bouguer Anomaly (MBA; Fig. S1B) by subtracting the gravity effects of the water layer above the seafloor and a constant crustal thickness of 6 km from the satellite-derived Free-Air Anomaly (FAA; Fig. S1A) (Sandwell and Smith, 2009), using GMT software gravity calculation ‘gravfft’ model (Wessel et al., 2019). The densities of water, crust, and mantle are assumed to be 1.03, 2.7, and 3.3 g/cm<sup>3</sup>, respectively, and the sediment layer near the ridge axis (<100 m thick) is negligible in the study area (Parnell-Turner et al., 2018). We then calculate the map of residual MBA (RMBA; Fig. S1C) by removing the gravity effect of lithosphere cooling relating to crustal ages from the MBA. The map of relative crustal thickness is inverted by the downward continuation of the RMBA, applying a cut-off filter at wavelengths between 20 and 30 km. Our results align well with the previous map of crustal thickness based on ship-based FAA (Smith et al., 2008). We assume that the average crustal thickness along the MAR 14°N segment is 6 km and build the map of relative crustal thickness (Fig. 1C).

### Faults and fissures detection

AUV high-resolution (HR) bathymetry (Fig. 2) and calculated slope maps (Fig. S3) are used to identify faults and fissures by a single analyst (J.C.). Faults and fissures in Area-1 are partly adapted from the previous study (Chen et al., 2025). Faults are linear and digitized as closed polygons along scarp tops and bottoms, according to sharp changes in bathymetry and slope. Fault relief is determined by the depth difference between the top and the bottom of the scarp, ranging from a few m to >300 m. Fissures are digitized along their margins, corresponding to linear depressions. Fissure width ranges from a few m to <50 m. This analysis yields 2554 faults and 1190 fissures in total (Table S1).

We measure the fault relief and fissure width based on cross-axis transects spaced at 2 m. Fault dip (defined as the largest value along the fault scarp) and spacing of faults and fissures are measured accompanied with the measurement of fault relief. The cumulative frequencies of the maximum fault relief and of the fault length follow exponential laws (log-linear plots in Fig. S5), suggesting that our picking process and measurements record small fault scarps. The plots of fault dip and its median value versus fault relief for 4 areas (Fig. S4) show that the median value of the fault dip increases from 10° to 60-80° as the fault relief increases

from 0 to  $\sim$ 50 m. The fault dip mostly stabilizes on 60–80° at reliefs over 50 m. The average fault-fissure spacing of the 4 areas is 136 m, with variations among individual areas ranging from 110 to 165 m.

### **Apparent tectonic strain calculation**

The map of apparent tectonic strain (ATS) is calculated by summing the fault heave ( $H$ ) and the fissure width ( $W$ ) over a moving circular window (Chen et al., 2025). Fault heave is based on measured fault relief ( $R$ ), expressed as:

$$H = R/\tan(\alpha),$$

where  $\alpha$  is the fault dip, treated as uniform values of 65° and 75° (Fig. 3 and S8). ATS in a circular window is expressed as:

$$ATS = 100\% \times C \cdot (\Sigma H + \Sigma W) / \pi r^2,$$

where  $r$  is the search radius of the moving circular window,  $\Sigma H$ , and  $\Sigma W$  are accumulations of fault heave and fissure width within the search window, respectively, and  $C$  is the spacing of cross-axis transects (2 m). The search radius ( $r$ ) is given as 200 m, constrained by the spacing of faults and fissures. We use the combination of  $r = 200$  m and  $\alpha = 65^\circ$  in Fig. 3, and to evaluate the robustness of our ATS calculation, we test other combinations of  $r$  (100 and 400 m) and  $\alpha$  (75°) in Fig. S8.

Area	1	2	3	4	All
Spreading rate (km/Ma)	27				
Surface area of high-resolution bathymetry data (km <sup>2</sup> )	19.4	11.45	13.67	33.85	78.37
Gravity crustal thickness (km)	6.8	6.4	5.9	5.5	-
Mean depth (km)	3.07	3.15	3.43	3.92	-
No. picked faults/fissures	1034/427	340/178	486/230	694/355	2554/1190
Average ATS inside axial valley at $\alpha=65^\circ$ (%)	7.6	5.1	4.3	2.7	5.3

**Table S 1. Information of high-resolution bathymetry data of the 4 areas at the MAR 14°N segment.** ATS: apparent tectonic strain.

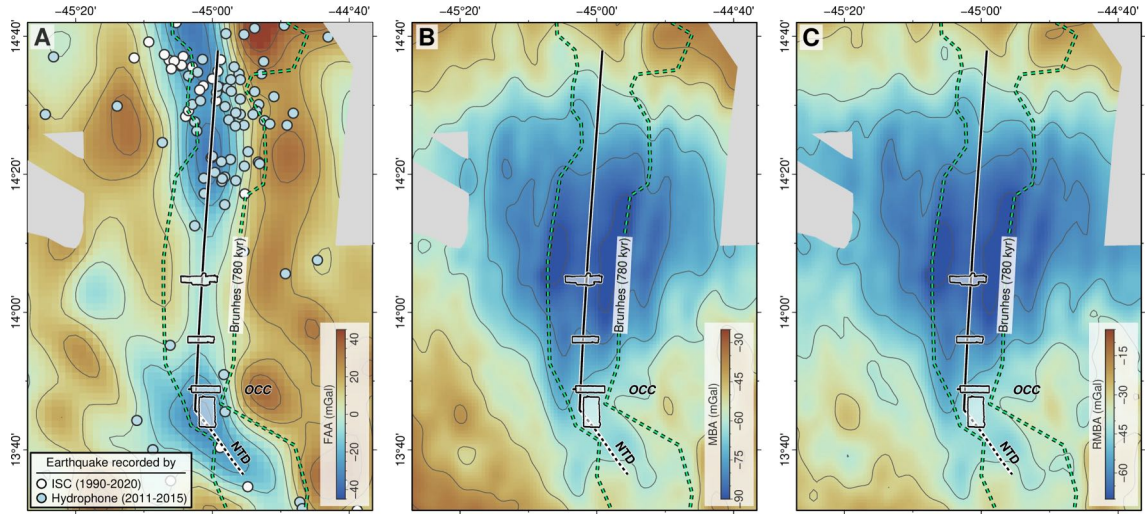


**Figure S 1. Gravity maps of the MAR 14°N segment.** See legend of geological interpretation in Fig. 1. **(A)** Free-air anomaly (FAA), based on satellite data (Sandwell and Smith, 2009). White and blue circles are earthquakes recorded by the International Seismological Centre (ISC) and hydrophones (Parnell-Turner et al., 2022), respectively. **(B)** Mantle Bouguer Anomaly (MBA). **(C)** Residual MBA (RMBA).

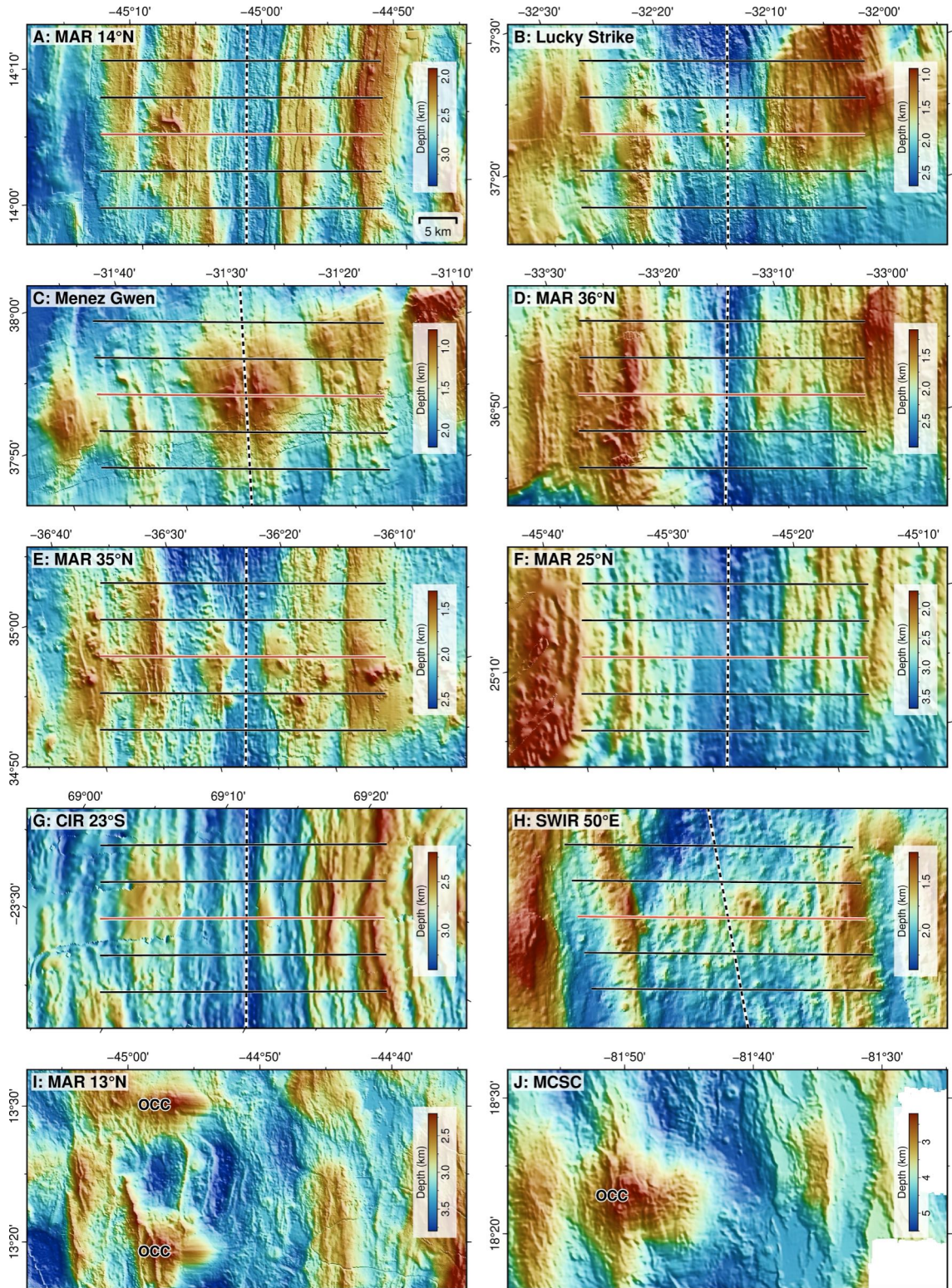


**Figure S 2. Ship-based bathymetric maps of 8 magmatic segments at slow-ultraslow spreading ridges.** All maps have the same distance scale. Dash line represents the ridge axis. Solid lines represent cross-sections for estimating apparent tectonic strain (see Fig. 5E and S9). Red lines represent cross-sections across segment centers.

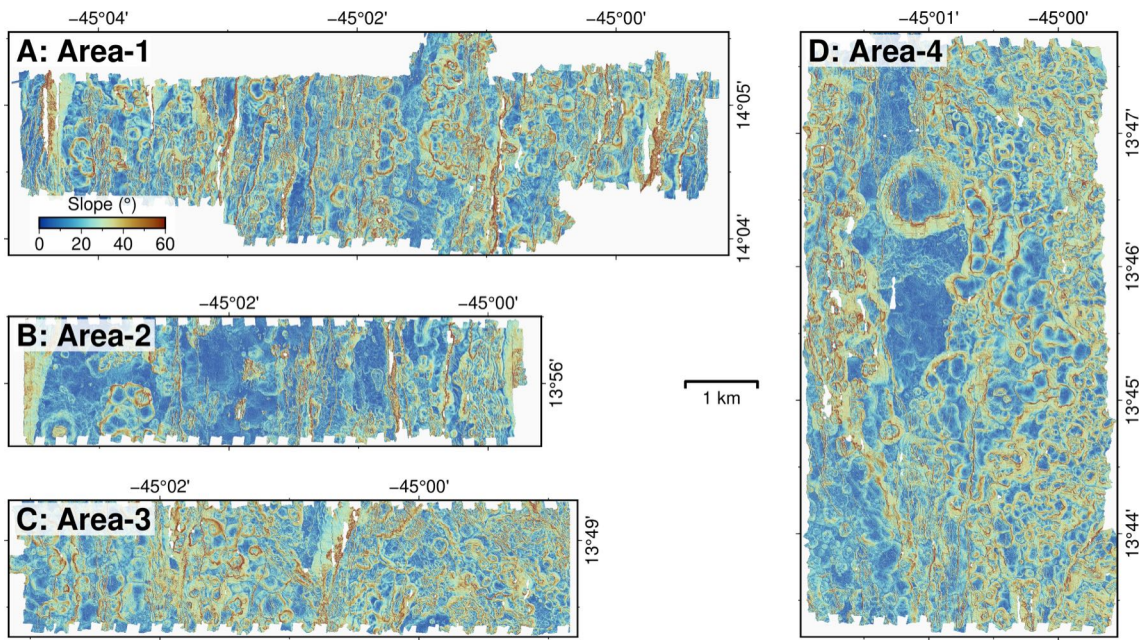
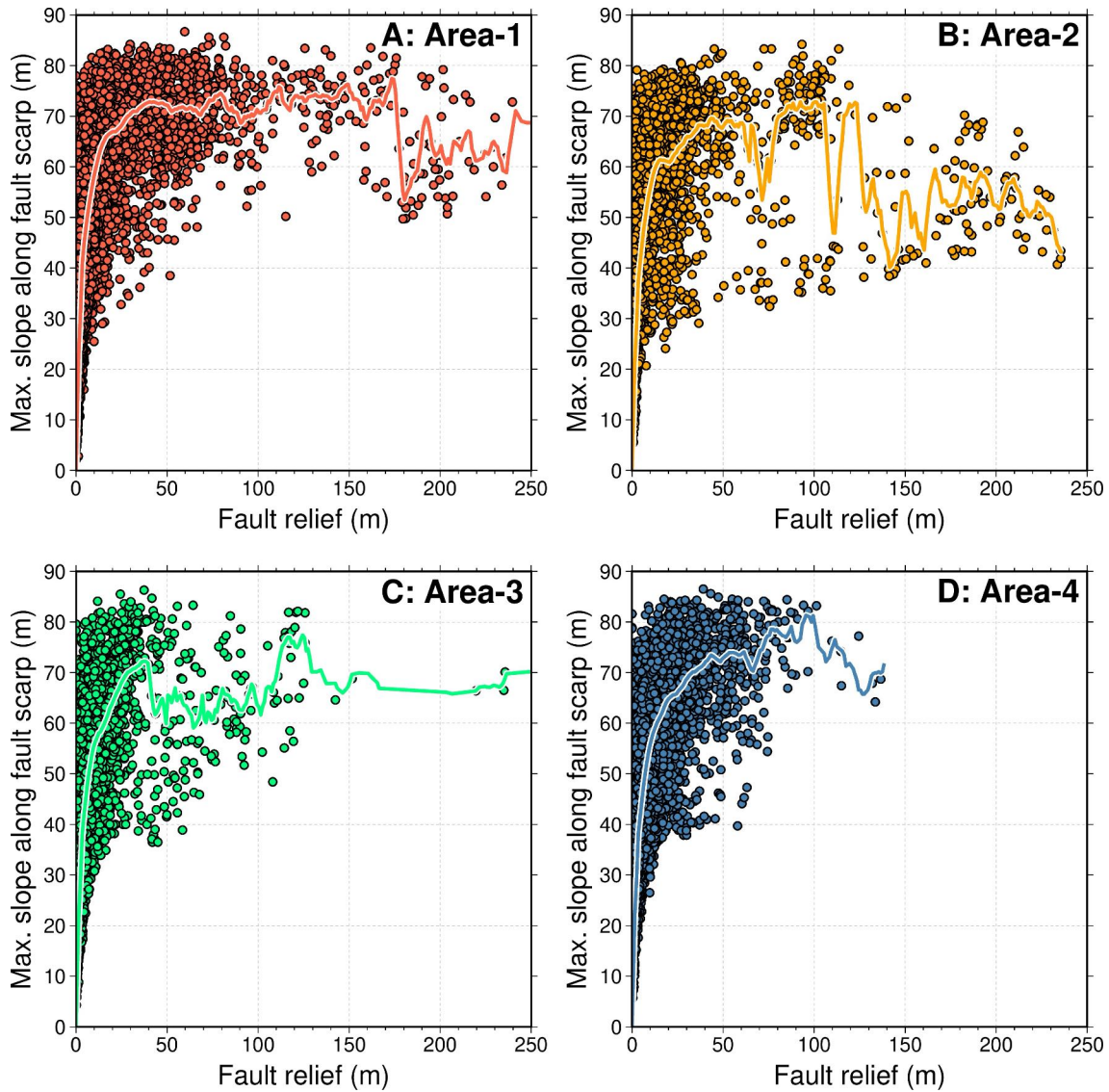
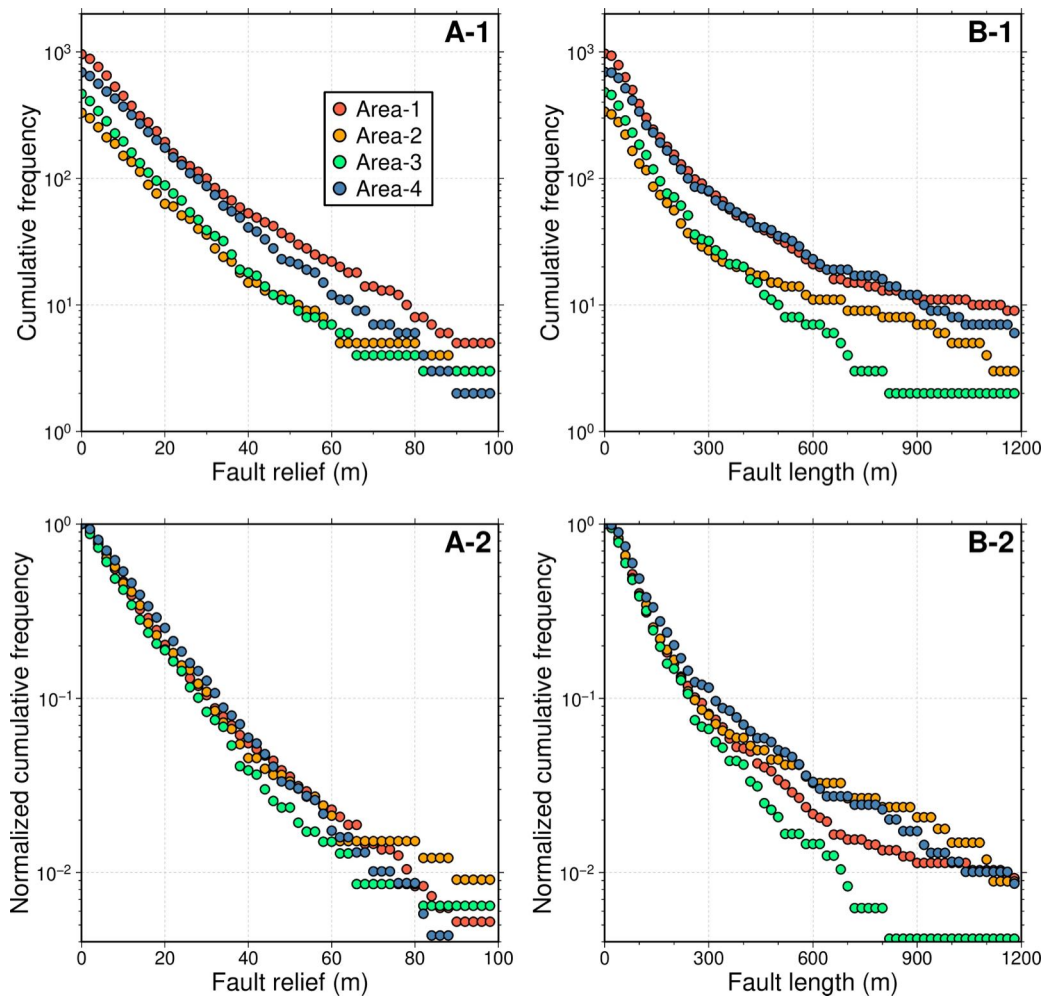


Figure S 3. **High-resolution slope maps of the Areas 1-4.** All maps are at the same distance and displayed with the same color scale for slopes.



**Figure S 4. Measured fault dip (dots) and median of fault dip (lines) versus fault relief of the Areas 1-4.** Most fault dips stabilize on  $60\text{--}80^\circ$  at reliefs over 50 m.



**Figure S 5. Log-linear plots for cumulative frequency of maximum fault relief and fault length.** Partially mapped faults are excluded from the statistics. Bins of relief and length are 2 m and 20 m, respectively. (A-1) and (B-1) Cumulative frequency. (A-2) and (B-2) Normalized cumulative frequency.

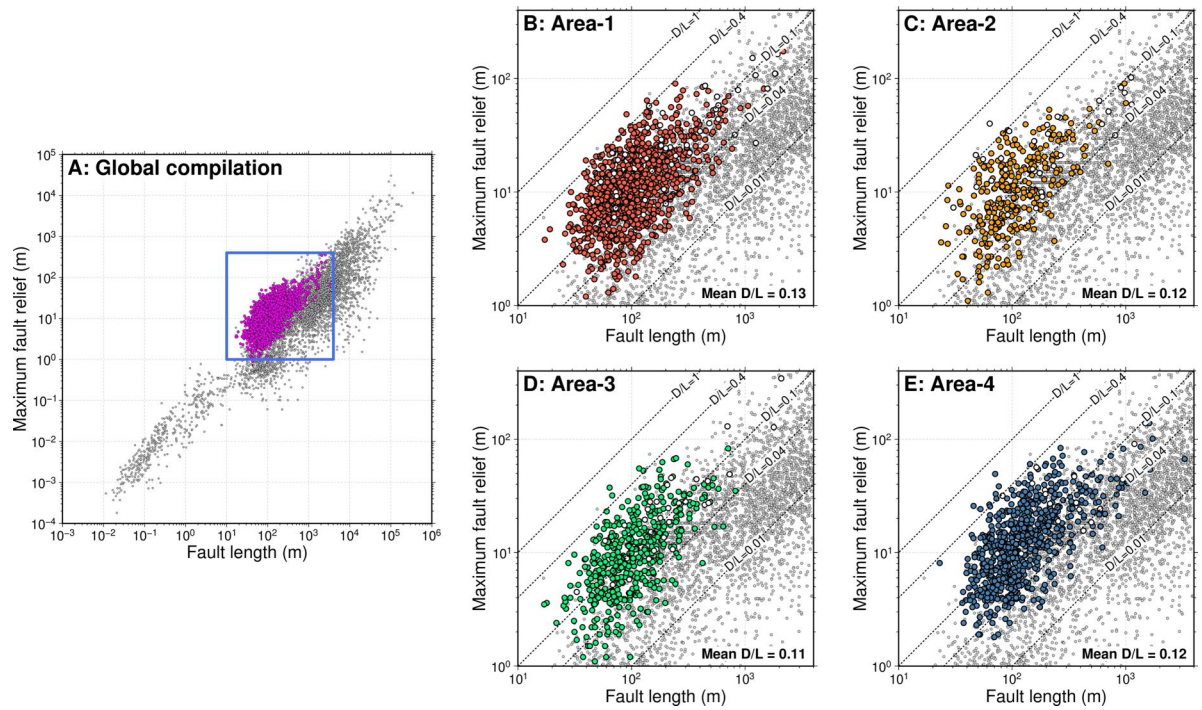


**Figure S 6. Maximum fault relief versus fault length (D/L ratio).** (A) Global compilation in gray dots (Lathrop et al., 2022) and 4 areas of this study in magenta. Blue square is the range in (B)-(E). Partially mapped faults are shown in open dots. The mean D/L ratio is 0.11-0.13 among the 4 areas.

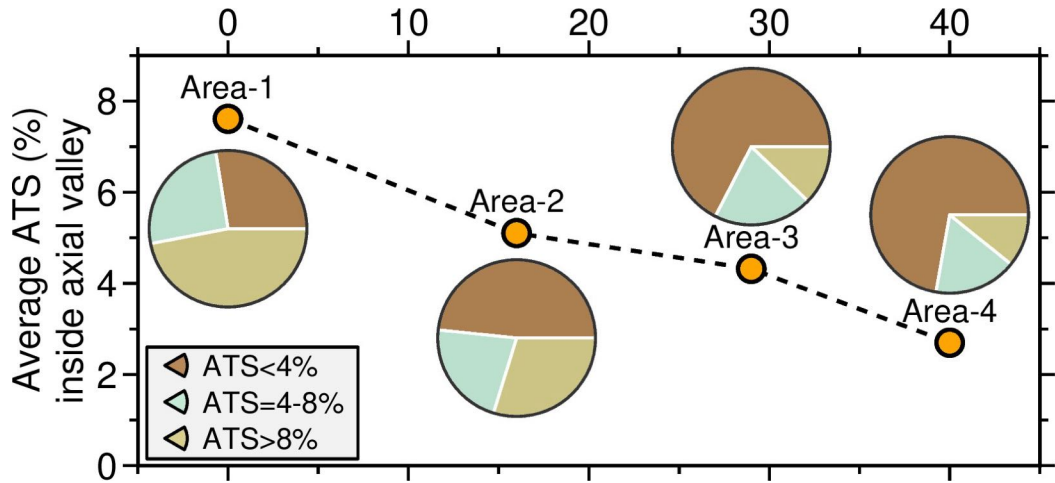


Figure S 7. **Along-axis ATS distribution.** Pie chart shows the proportion of the Areas 1-4 at the ATS of <4%, 4-8%, and >8%.

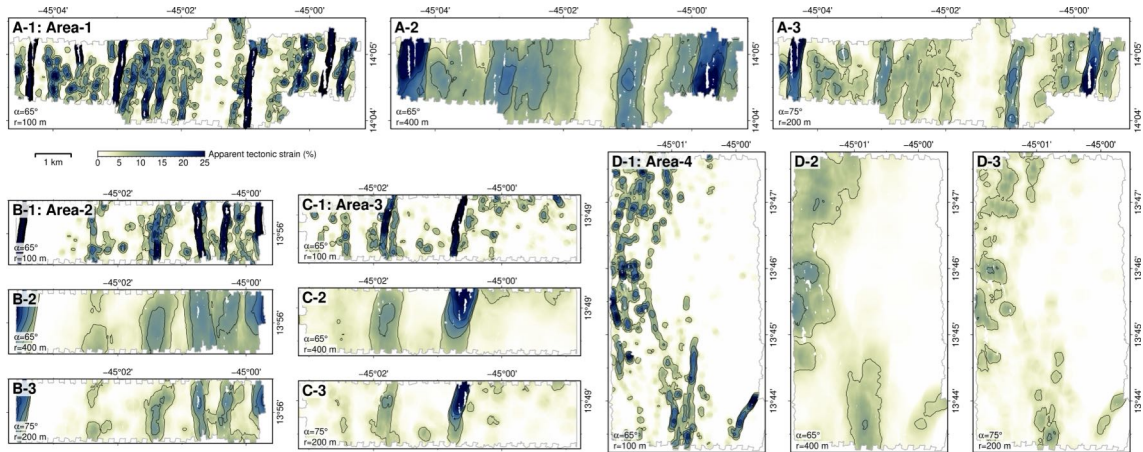
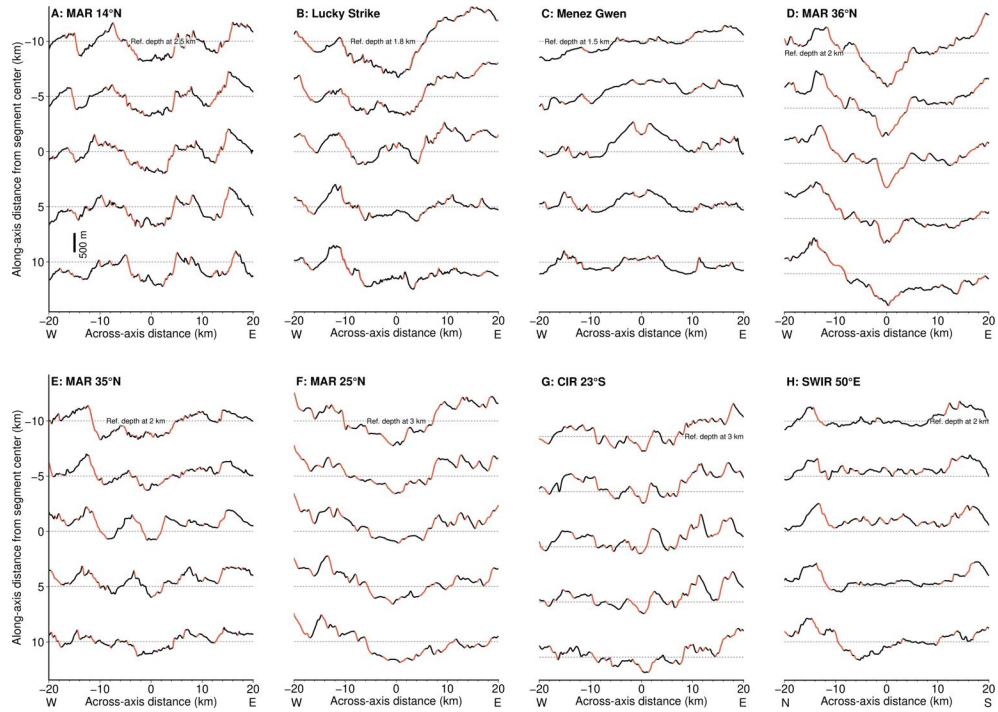
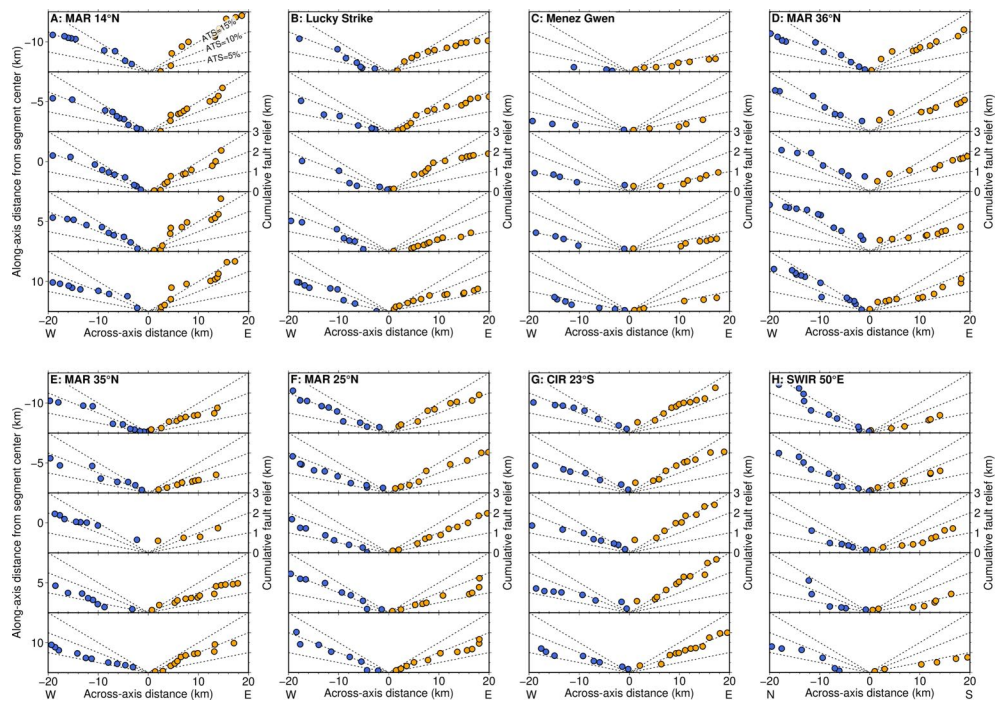


Figure S 8. **Apparent tectonic strain calculated using  $\alpha = 65/75^\circ$  and  $r = 100/200/400$  m of the Areas 1-4.** See the lower-left corner for values of  $\alpha$  and  $r$ . See the combination of  $\alpha = 65^\circ$  and  $r = 200$  m in Fig. 3.



**Figure S 9. Topographic cross-sections (VE=7.5) within 20 km off axis of 8 magmatic segments at slow-ultraslow spreading ridges.** See locations in Fig. S2. Fault scarps are shown in red. Horizontal dashed lines represent reference depths.



**Figure S 10. Cumulative fault relief versus distance, measured along cross-sections in Fig. S9.** Blue dots correspond to the west or north flanks, and orange dots correspond to the east or south flanks. Dashed lines make the ATS values at 5%, 10%, and 15%, using a uniform fault dip at 45°.

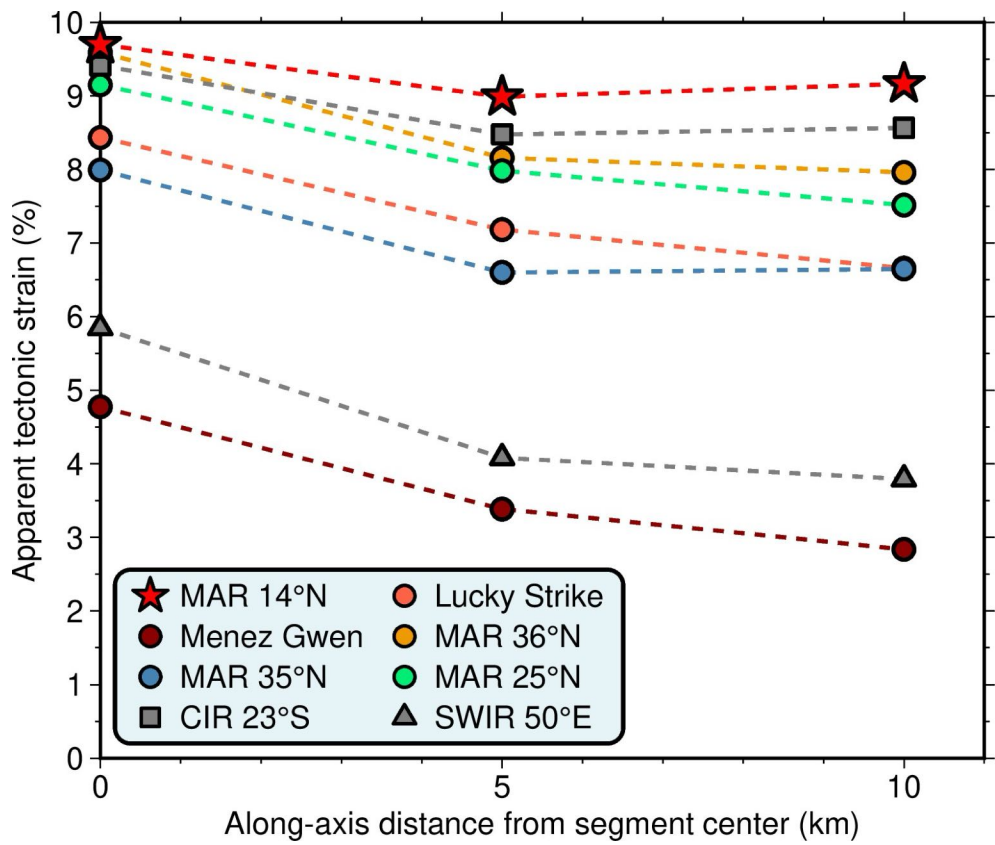


**Figure S 11. Apparent tectonic strain (ATS) of 8 magmatic slow-spreading ridge**

**segments.** See Fig. 5 for normalized ATS to segment centers. For this calculation, fault dip is assumed to be  $45^\circ$  at all sites and profiles.